ω photoproduction at the BGOOD experiment for most backward angles

Christian Tillmanns

Masterarbeit in Physik
angefertigt im Physikalischen Institut

vorgelegt der
Mathematisch-Naturwissenschaftlichen Fakultät
der
Rheinischen Friedrich-Wilhelms-Universität
Bonn

06 2021

I hereby declare that this thesis was formulated by myself and that no sources or tools other than those cited were used.

Bonn, ...

Date Signature

1. Gutachter: Prof. Dr. Hartmut Schmieden
2. Gutachter: Prof. Dr. Philip L. Cole

Acknowledgements

I would like to thank Prof. Hartmut Schmieden for the opportunity of this master thesis. Furthermore I want to thank all members of the BGOOD group for all the support I received with special thanks to Dr. Georg Scheluchin.

Contents

CHAPTER 1

Introduction

Throughout history, mankind was intrigued by the search for the fundamental rules and building blocks of the universe. The ancient Greeks introduced the concept of tiny, indivisible particles, which make up all matter. This idea inspired scientists to discover the smallest unit of a chemical element, the atom. In 1911 the Rutherford experiment scattered α-particles on a thin gold foil and revealed, contrary to the Thomson model, that most of an atom's mass is concentrated in a small, positively charged nucleus. Soon it was discovered that the nucleus consists of nucleons that also have substructure. Intensified studies revealed the constituents of nucleons throughout the 20th century. These particles were hence known as quarks and are today part of the standard model. This model classifies all known elementary particles as leptons or quarks and explains fundamental forces with the exchange of gauge bosons. Quarks carry the colour charge of the strong interaction, which is described by quantum chromodynamics. Due to the colour confinement of the strong interaction quarks do not exist as free particles and are only found in bound states, called hadrons. These either consist of three quarks for baryons or a quark antiquark pair for mesons. Different quark combinations and excitations of these hadrons give rise to a large variety of particles. Although experiments found many hadronic states, many more resonances are predicted than have been observed. One possible explanation for these "missing resonances" is the weak coupling to the πN channel [1], since many experiments made use of πN scattering. It is assumed to find these unobserved states in non-pionic reaction channels. Therefore photoproduction experiments are suited for this endeavour. One reaction with potential to find new resonances is the $\gamma p \rightarrow \omega p$ reaction channel. Experiments studying this channel revealed different contributions of reaction mechanisms. For a better understanding of these contributions, all kinematical regions need to be considered. Published differential cross section data of this reaction for most backward angles of the ω meson near threshold are scarce. Therefore this thesis determines the differential cross section in this kinematical region. One experiment that is suited for such investigations is the BGOOD experiment in Bonn. It utilises energy-tagged real photon beams up to 3 GeV energy to produce mesons on a fixed proton or neutron target. It consists of a central detector surrounding the target and a forward spectrometer providing good identification for charged particles in the forward direction.
In this thesis, the $\gamma p \rightarrow \omega p$ reaction channel is reconstructed and the differential cross section for most backward angles of the ω meson determined. At first, chapter 2 gives an introduction to the $\gamma p \rightarrow \omega p$ reaction channel, including the basic kinematics and an overview of the reaction mechanisms. After this, the research status is presented in chapter 3. Chapter 4 describes the BGOOD

setup and chapter 5 goes over two analysis tools that are applied in this thesis. The reconstruction including the cut selection and yield extraction is discussed in chapter 6. Subsequently, chapter 7 shows the determination of the differential cross section and presents the results. Finally, the last chapter 8 gives a summary of this thesis.

CHAPTER 2

Kinematics and reaction mechanisms

This chapter introduces the $\gamma p \rightarrow \omega p$ reaction channel. First, an overview of the ω meson is given in section 2.1. After this, some basic kinematic relations are described in section 2.2 and the relevant reaction mechanisms shown in section 2.3.

2.1 The ω meson

The ω meson has a spin and parity of $J^P = 1^-$ [2] and is, therefore, a vector meson. Since it consists only of up and down quarks

$$|\omega\rangle = \frac{1}{\sqrt{2}} \left[|d\bar{d}\rangle + |u\bar{u}\rangle \right] \tag{2.1}$$

this neutral particle is similar to the ρ meson but represents the singlet with isopin 0. Its mass is $m_\omega \approx 783$ MeV [2] with a narrow decay width of $\Gamma \approx 8.49$ MeV [2]. This decay width corresponds to a mean lifetime of $\tau_\omega \approx 7.75 \cdot 10^{-23}$ s [2]. The two most dominant decay channels are via the strong interaction with a branching ratio of $\Gamma_i/\Gamma \approx 89.3\%$ [2]

$$\omega \rightarrow \pi^+\pi^-\pi^0 \rightarrow \pi^+\pi^-\gamma\gamma \tag{2.2}$$

and via the electromagnetic interaction with a branching ratio of $\Gamma_i/\Gamma \approx 8.4\%$ [2]

$$\omega \rightarrow \pi^0\gamma \rightarrow \gamma\gamma\gamma. \tag{2.3}$$

Both channels include a π^0 meson which decays with a mean lifetime of $\tau_{\pi^0} \approx 8.43 \cdot 10^{-17}$ s [2] and corresponds to a distance of 25.3 nm. Therefore only its decay particles which are almost always two photons with a branching ratio of $\Gamma_i/\Gamma \approx 98.8\%$ [2] can be detected.

2.2 Kinematic relations

In meson photoproduction $\gamma p \rightarrow \omega p$, the energy and momentum of the particles can be described with four-momentum notation. For a particle A, its quantities are written as

$$\mathbf{A} = \begin{pmatrix} E \\ p_x \\ p_y \\ p_z \end{pmatrix} = \begin{pmatrix} E \\ \vec{p} \end{pmatrix} \tag{2.4}$$

with its mass given by the absolute value $m_{\mathrm{A}} = |\mathbf{A}| = \sqrt{E^2 - \vec{p}^2}$.
With this the four-momentum of the initial particles assuming the proton $\boldsymbol{p_i}$ is at rest and the initial beam photon $\boldsymbol{\gamma_i}$ is moving along the z-axis is

$$\begin{pmatrix} E_\gamma \\ 0 \\ 0 \\ E_\gamma \end{pmatrix} + \begin{pmatrix} m_p \\ 0 \\ 0 \\ 0 \end{pmatrix} = \boldsymbol{\gamma_i} + \boldsymbol{p_i} \tag{2.5}$$

For photon energies E_γ above the ω production threshold of $E_\gamma^{\omega\ \mathrm{thres}}$ ≈1109 MeV the four-momentum conservation of the reaction in the case of the most dominant decay can be written as

$$\boldsymbol{\gamma_i} + \boldsymbol{p_i} = \boldsymbol{p_f} + \boldsymbol{\omega} = \boldsymbol{p_f} + \boldsymbol{\pi^+} + \boldsymbol{\pi^-} + \boldsymbol{\pi^0} = \boldsymbol{p_f} + \boldsymbol{\pi^+} + \boldsymbol{\pi^-} + \boldsymbol{\gamma_f^1} + \boldsymbol{\gamma_f^2}. \tag{2.6}$$

This relation leads to two quantities that will be further used in this thesis.
The absolute value of a four-momentum vector is referred to as the invariant mass. For the two photons produced by the decay of the π^0 this results in the

$$\text{invariant mass of } \gamma_f^1\gamma_f^2 : |\boldsymbol{\gamma_f^1} + \boldsymbol{\gamma_f^2}| = m_{\pi^0} \tag{2.7}$$

A similar approach is used for the missing mass by determining the four-momentum of particles that were not detected. The missing mass takes the initial state and subtracts the four-momentum of detected particles so that the resulting difference corresponds to the missing four-momentum. As an example, the missing mass to the proton will be defined as

$$|\boldsymbol{\gamma_i} + \boldsymbol{p_i} - \boldsymbol{p_f}| \tag{2.8}$$

which, for the given reaction, corresponds to the ω meson mass m_ω.

2.3 Reaction mechanisms

At high energies, the reaction $\gamma p \rightarrow \omega p$ is dominated by diffractive scattering. The Feynman diagram for this process can be seen in figure 2.1 a). The photon is converted into an ω meson which is lifted on the mass shell by scattering off a proton by exchange of a pomeron. For lower energies, the t-channel meson exchange becomes a dominant contribution. Figure 2.1 b) shows the Feynman diagram of this process. It was suggested that π^0- and f_2-meson exchange are the most dominant [3]. At energies around the ωp production threshold, N^* resonances too are expected to contribute. The Feynman diagrams for those can be seen in figure 2.1 c) and d). Here only N^* resonances occur since Δ^* contributions are filtered out by the isospin I= 0 of the ω meson. Considering the polar angle θ_{CMS} of the ω in the center of mass frame for lower photon energies, the t-channel with small momentum transfer t dominates the forward angles. The most backward angle region with large momentum transfer t is expected to contain u-channel contributions.

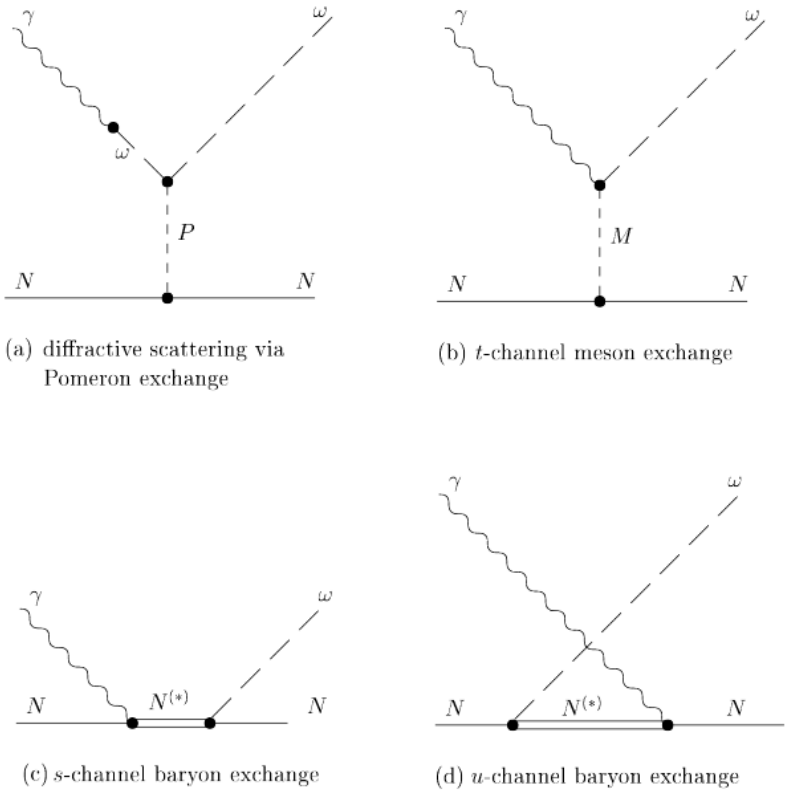

Figure 2.1: Processes involved in ω meson photoproduction [4]

CHAPTER 3

Research status

The photoproduction of the ω meson has been studied by several experiments. The SAPHIR Collaboration published differential cross section and spin density matrix elements. Their data showed that diffraction is no longer dominant for center of mass energies below 2.4 GeV and that resonances must play an important role [5]. Beam asymmetry data from the CBELSA/TAPS Collaboration indicated s-channel resonance formation on top of the t-channel exchange process [6]. The GRAAL Collaboration confirmed the importance of resonant states with their measurement of the Σ beam asymmetry for ω photoproduction [7]. The CLAS Collaboration reported high statistics differential cross section and spin density matrix elements [8] and performed a partial wave analysis on this data set, which showed dominance of the t-channel π^0 exchange in forward direction [9]. Later the CBELSA/TAPS Collaboration published differential cross section with ω photoproduction off hydrogen and deuterium [10]. Shortly after, another study for the differential cross section and spin density matrix was reported by the CBELSA/TAPS Collaboration [11]. It found pomeron exchange at higher energies as dominant contribution and was able to describe the data by combining the pomeron exchange, t-channel contributions and resonances. The A2 Collaboration at MAMI reported differential cross section with full production angle coverage [12]. Differential cross section for backward angles was published by the LEPS Collaboration [13].

Partial wave analyses agree with the important role of resonance contributions, but identify various resonances as the dominant contribution. Q. Zhao [14] uses an effective Lagrangian approach and finds N(1720) and N(1680) as dominant resonances. In Ref. [15] a quark model by Capstick and Roberts is used to identify N(1960) and N(1910) as dominant contributions. Ref. [16] finds with an effective Lagrangian approach and vector dominance model that the dominant resonances are N(1680) and N(1520). A coupled-channel analysis in Ref. [17] shows N(1710) and N(1900) to dominate the ωN production mechanism. The partial wave analysis of the CLAS Collaboration [9] mentioned before concluded that N(1680), N(1700) and N(2190) are the dominant resonance contributions. In Ref. [18] twelve branching ratios for $N^* \rightarrow \omega N$ were determined. Another effective Lagrangian approach was used in Ref. [19] to describe CLAS data by considering the resonances N(1520), N(1700), N(1720), N(1860), N(1875), N(1895) and N(2060).

Overall there is agreement on the dominance of the diffractive process for high energies and the important role of the t-channel for lower energies. In this energy region, s-channel resonances also contribute, but u-channel resonance contributions are not conclusively resolved.

The following provides a brief description of the experiments which published differential cross

sections. The experimental setup and methods that were used are summarised for a better interpretation of the data.
All experiments are using energy tagged real photon beams. The detector systems vary for each experiment, which results in a different coverage of energy and angular regions.

3.1 SAPHIR

The SAPHIR experiment combines drift chambers and a scintillator wall for momentum and time-of-flight measurements of charged particles. Tracks of charged particles produced by the interaction between the bremsstrahlung photon with the liquid hydrogen target are measured by a magnetic spectrometer surrounding the target. Using drift chambers the curvature of the tracks can be determined and from this the particle momentum. Combined with the time-of-flight information the mass can be identified. The SAPHIR experiment can only detect charged particles but over a large angular range.
In 2003 the SAPHIR Collaboration at the Bonn electron stretcher ring ELSA published data for the differential cross section of the ωp channel for photon energies from threshold up to $E_\gamma = 2.4$ GeV and full angular range [5].
For this cross section data the decay channel $\omega \to \pi^+\pi^-\pi^0$ was selected and kinematic fits applied. The separation of background and signal was mostly done by fitting a polynomial of 3rd order summed with a convolution of a Breit-Wigner and two Gaussians.
The resulting data show that t-channel π^0 exchange dominates the differential cross section at the higher beam energies of the experiment and suggests s-channel resonance contributions close to threshold.

3.2 CLAS

The CLAS experiment at Jefferson Lab measures the momentum of emerging particles using a nonuniform toroidal magnetic field in conjunction with drift chamber tracking. Additionally, the time-of-flight is measured by scintillators outside the range of the magnetic field. This is further complemented by a calorimeter for photons. The CLAS experiment has a good momentum resolution for charged particles over a large angular range.
The CLAS Collaboration published ω photoproduction data with high precision in most angular regions in 2009 [8]. It covers energies between threshold and $W = 2.84$ GeV with narrow energy steps and the angular range $-0.8 < \cos(\theta_{\mathrm{CMS}}) < 0.96$ in small steps.
The $\pi^+\pi^-\pi^0$ decay was used since the CLAS experiment is optimised for charged particles. One-constraint kinematic fits are used for channel selection. For background separation, a method was developed that assigns a signal weight factor Q to each event, which was used for most likelihood fits. The results show a strong contribution of t-channel for high energies and very forward angles.

3.3 CBELSA/TAPS

The CBELSA/TAPS experiment at the Bonn electron stretcher ring ELSA measures particles with a hermetic electromagnetic calorimeter consisting of a central barrel around the target cell and a forward wall. For the identification of charged particles, a scintillating fiber detector is used in

combination with the central calorimeter and a hexagonal plastic veto detector for the forward wall. The CBELSA/TABS experiment detects photons over a large angular range.
2014 the CBELSA/TAPS Collaboration published ω photoproduction off protons and neutrons data with photon energies from threshold up to $E = 2$ Gev [10] covering the complete angular range.
The reaction channel was identified via the $\pi^0\gamma \rightarrow \gamma\gamma\gamma$ decay. For the reduction of background, a cut on the missing mass to the three photons was applied. The simulation of the signal motivated a cut depending on the correlation of the opening angle between π^0 and γ and the momentum of the ω in center of mass system. Additionally, a cut on the kinematical constraints of the polar angle in the lab system depending on the beam energy was made. For the final separation of background, a fit was performed that summed a Gaussian with a background function with five parameters.
The resulting data further indicate t-channel production for forward angles. This data set will be referred to as CBELSA 2014.
Another data set of differential cross section data for the ωp channel was published by the CBELSA/TAPS Collaboration in 2015 [11]. It includes the full angular range and initial photon energies from threshold to 2.5 GeV.
The $\pi^0\gamma \rightarrow \gamma\gamma\gamma$ reaction channel was selected and reconstructed by kinematic fitting with the proton as a missing particle. The ω yield was extracted with a similar method as described in the previous paper.
The results showed pomeron exchange as a dominant contribution at higher energies and were able to describe the data by combining the pomeron exchange, t-channel contributions and resonances. This data set will be referred to as CBELSA 2015.

3.4 LEPS

The experimental setup at the LEPS facility in Sayo Town, Japan detects particles with a forward spectrometer. It consists of a dipole magnet, multiwire drift chambers, a start counter, a Cerenkov counter and a time-of-flight hodoscope. Additionally, a time projection chamber (TPC) for charged particles that surrounds the target was installed inside a solenoid magnet. The LEPS experiment has a good angular resolution for charged particles in the forward and central direction.
The LEPS Collaboration published data for the differential cross section of ω photoproduction at backward angles $-1 < \cos(\theta_{\mathrm{CMS}}) < -0.8$ and beam energy range 1.5 GeV $< E_\gamma <$ 3 GeV in 2014 [13]. For the identification of the ω meson the decay $\pi^+\pi^-\pi^0$ channel was selected. The proton needed to be measured by the forward spectrometer and the charged pions in the TPC. For the π^0, the missing mass information was used and a cut applied. One or two charged particles were required and a cut on the proton mass and momentum was used. For background separation, different reactions including the signal were simulated and fitted as a superposition to the experimental data (template fit).
The results show a larger differential cross section for energies between $W = 2.0$ GeV and $W = 2.4$ GeV than the expected u-channel contribution in this angular region.

3.5 Crystal Ball

The Crystal Ball experimental setup at MAMI uses a central calorimeter and forward calorimeter. Particles emerging from the target cell are detected by the Crystal Ball surrounding the target or by TAPS for forward angles. The detector setup is similar to the CBELSA/TABS experiment with similar

coverage for particles.
The A2 Collaboration at MAMI published differential cross section data for the ω photoproduction in 2015 [12]. The data cover photon energies from threshold up to E_γ 1.4 GeV with narrow energy steps and the complete angular range.
The differential cross section was determined via the $\pi^0\gamma \rightarrow \gamma\gamma\gamma$ reaction channel. Event selection was performed with kinematic fitting techniques. For background separation, a function combining a Gaussian, representing the signal, and a polynomial function for the background was fitted.

3.6 Data comparison

For a comparison of the currently available differential cross sections at most backward angles two example energy regions are shown in figure 3.1. The differential cross section for photon energies around $E_\gamma \approx 1284$ MeV can be seen in figure 3.1(a). In general, a satisfactory agreement is observed between the different data sets. Only for most backward angles, variations can be seen. Crystal Ball data suggest a flat distribution towards backward angles, while SAPHIR data show lower and CBELSA 2015 data higher differential cross section values. CLAS data cover only the angular region of $-0.8 < \cos(\theta_{\mathrm{CMS}}) < 0.8$ and CBELSA 2014 data show limited angular resolution for most backward angles. A significant increase of differential cross section in this region might imply u-channel resonance contribution.
Figure 3.1(b) compares the differential cross sections at photon energies around $E_\gamma \approx 1834$ MeV. An overall agreement between CLAS, CBELSA 2014 and LEPS data can be observed. CBELSA 2015 data lie above the rest for $\cos(\theta_{\mathrm{CMS}}) < -0.5$. CLAS data show a decrease in differential cross section towards more backward angles, which is continued with LEPS data for most backwards angles.
For further studies of possible u-channel contributions more precise data for most backward angles are needed. Therefore this thesis extracts the differential cross section of the $\gamma p \rightarrow \omega p$ reaction for energies between threshold and $E_\gamma \approx 2$ GeV and $-0.99 < \cos(\theta_{\mathrm{CMS}}) < -0.9$. It requires an experimental setup capable of meson photoproduction at extreme angles. This is provided by the BGOOD experiment which is described in the next chapter.

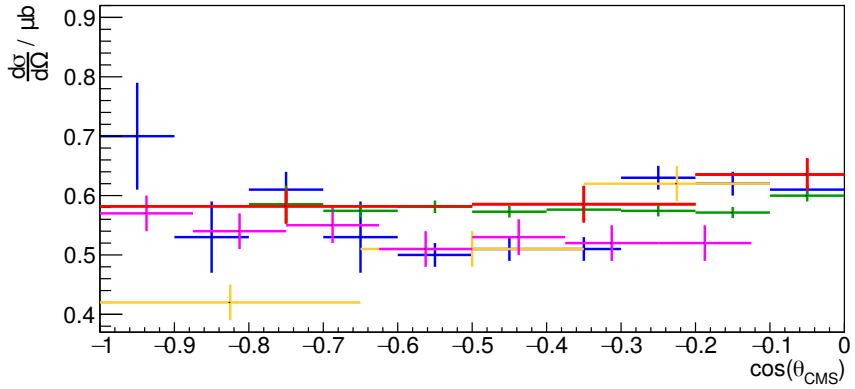

(a) Differential cross section $\frac{d\sigma}{d\Omega}$ against $\cos(\theta_{\mathrm{CMS}})$ of the ω meson in the incident photon energy range 1259 MeV < E_γ < 1309 MeV. In red/blue the CBELSA 2014/2015 [10] [11] data, in green CLAS [8] data, in magenta Crystal Ball [12] data and in yellow SAPHIR [5] data.

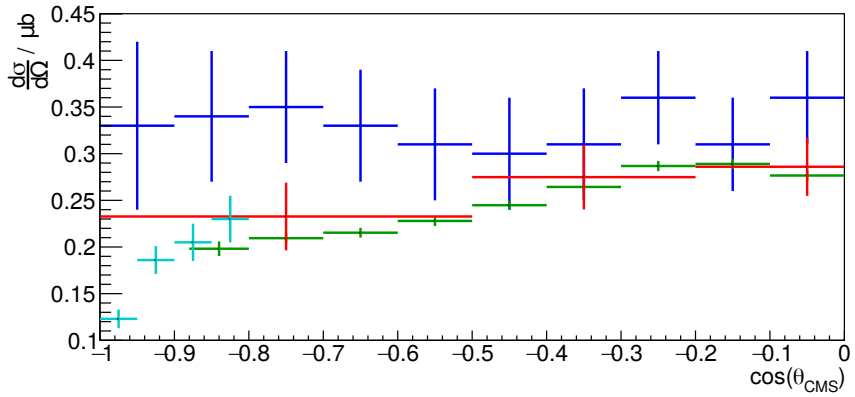

(b) Differential cross section $\frac{d\sigma}{d\Omega}$ against $\cos(\theta_{\mathrm{CMS}})$ of the ω meson in the incident photon energy range 1809 MeV < E_γ < 1859 MeV. In red/blue the CBELSA 2014/2015 [10] [11] data, in green CLAS [8] data and in cyan LEPS [13] data.

Figure 3.1: Differential cross section $\frac{d\sigma}{d\Omega}$ against $\cos(\theta_{\mathrm{CMS}})$ of the ω meson for two different incident photon energy regions E_γ from different experiments.

CHAPTER 4

BGOOD experiment

The BGOOD experiment is located at the **El**ectron **S**tretcher **A**ccelerator (**ELSA**) facility beneath the Physikalisches Institut of the Universatity of Bonn. This fixed target experiment is ideally suited for meson photoproduction at extreme angles. With the combination of a central detector and a forward spectrometer, excellent angular acceptance is achieved. Its name consists of the material of the central calorimeter **B**ismuth **G**ermanate **O**xide and the **O**pen **D**ipole magnet, which is the heart of the forward spectrometer.
In section 4.1 the ELSA accelerator is described. Section 4.2 goes over the most important parts of the BGOOD experiment. A more detailed description can be found in Ref. [20].

4.1 ELSA

To induce meson photoproduction photon energies in the GeV region are required. To achieve this accelerated electrons from ELSA are used. An overview of this accelerator can be seen in figure 4.1. This accelerator produces electrons up to 3.2 GeV as a quasi-continuous beam and is able to generate polarised electrons if needed.
The first stage consists of an electron gun to free electrons via thermionic emission and a linear accelerator (LINAC) to accelerate the electrons to around 20 MeV. In the next stage, the electrons are transferred to the booster synchrotron. There they reach energies between 0.5 GeV and 1.6 GeV, before they get injected as bunches into the stretcher ring. In this third stage energies of up to 3.2 GeV can be realised and a small part of the beam is redirected to the BGOOD or Crystal Barrel experiment, resulting in a quasi-continuous beam.

4.2 BGOOD experiment

A schematic overview of the BGOOD experiment can be found in figure 4.2. The ELSA electron beam is guided to a goniometer tank holding different radiators at the start of the BGOOD setup. The electrons create a real photon beam via bremsstrahlung with unpolarised or linear polarised photons depending on the selected radiator. These photons get energy-tagged and impinge on the target, which is liquid hydrogen for free protons or liquid deuterium as a neutron target. This setup allows for meson photoproduction, where the emerging particles can be observed by the main detection systems.

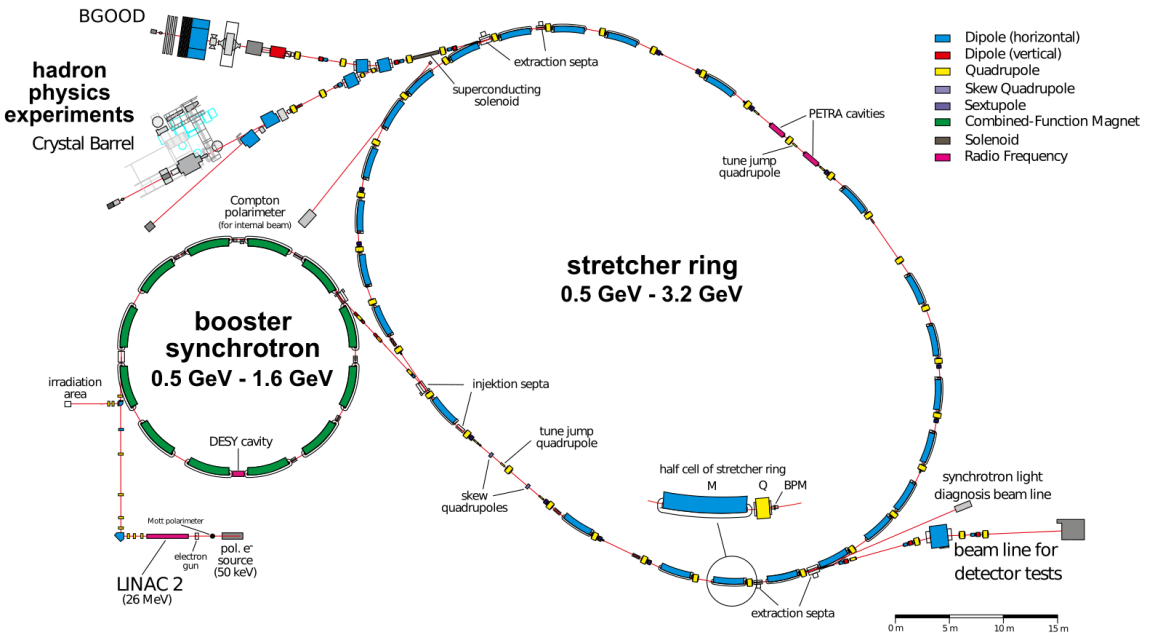

Figure 4.1: Overview of the ELSA accelerator facility [21]

The BGO-ball surrounds the target cell and is complemented by the intermediate detectors for more forward polar angles. Particles at most forward angles are detected by the forward spectrometer. The photon flux can be measured behind these systems.
For this setup, the angle between beam axis and particle direction is the polar angle θ and the angle around the beam axis is described by ϕ. Both angles can be represented in the center of mass system and will then be marked as θ_{CMS} and ϕ_{CMS}.
The next sections will focus on the different components of this setup in more detail.

4.2.1 Tagging System

With the tagging system, it is possible to measure the time and energy of the post bremsstrahlung electron to determine the initial photon and reconstruct the initial state for each reaction. In figure 4.3 an overview of the tagging system can be found. At first, the electron beam is guided onto a radiator. For unpolarised photons a copper radiator and for linear polarised photons a diamond radiator is used. The goniometer allows for a precise switching between them. For unpolarised photons, each electron interacts with one copper atom and emits a photon without preference of its orientation. When using the diamond radiator, in addition to this incoherent process, the electrons can also scatter coherently with the crystal lattice. This will result in a linear polarisation for a portion of the post bremsstrahlung photons.
After the goniometer tank particles enter the tagger magnet. There electrons will be deflected by the Lorentz force depending on their velocity. Photons will pass through unaffected to the target and electrons that did not undergo bremsstrahlung are guided into the beam dump. The remaining electrons hit one of the 120 plastic scintillators of the tagger hodoscope, so its energy can be determined. The tagger covers an energy range of 10% up to 90% of the initial electrons energy E_0 with resolution

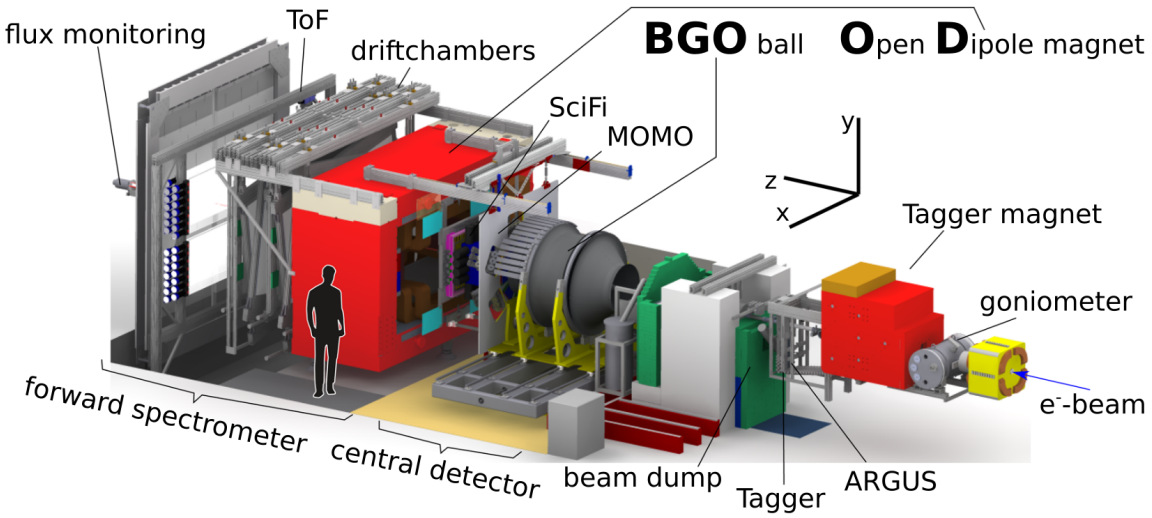

Figure 4.2: Overview of the BGOOD setup [20].

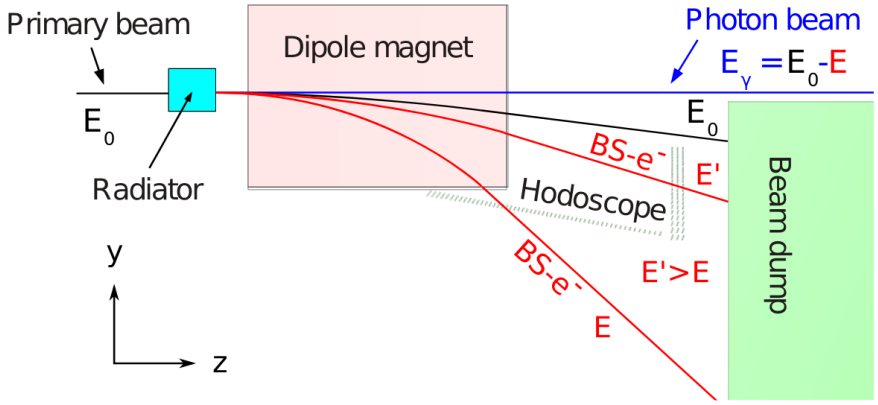

Figure 4.3: Components and working principle of the photon tagger [22].

around 0.5% E_0 for low energies and 2.2% E_0 for high energies [22]. Since the energy of the electron before E_0 and after bremsstrahlung E_B is known, the energy of the photon can be calculated with

$$E_\gamma = E_0 - E_B \tag{4.1}$$

With a solid time resolution, the hodoscope can thereby tag each photon hitting the target and the initial state of a reaction is known.
For a more precise measurement of the energy, the tagger is complemented by ARGUS [23] [24]. Its fiber scintillators are smaller compared to the tagger and result in a better resolution.

4.2.2 Central detectors

The tagged and collimated photons travel through the beampipe and impinge on the target cell in the center of the BGO ball. The target cell can hold liquid hydrogen or deuterium. Since for both of these targets temperatures around 20 K are needed a cryostat system is used. The target cell has a length of 5 cm and an effective length of 6.1 cm when the Mylar windows are accounted for. Alternatively, a solid target can be utilised. In order to detect reactions in this central region, three systems directly

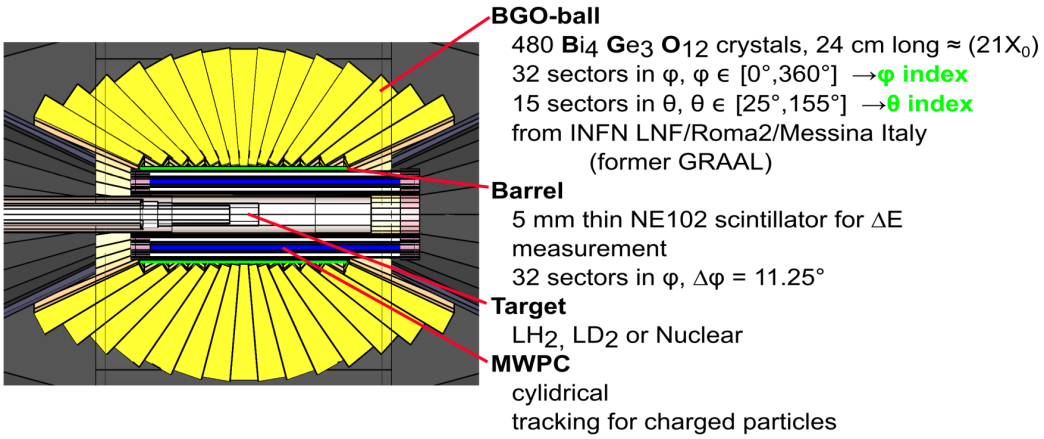

Figure 4.4: Slice view of the BGO ball. The Photon beam direction is from left to right. [25]

surround the target. They can be seen in the overview of the central detectors in figure 4.4 and will be described in the following.

MWPC

Directly around the target cell, two coaxial multi-wire proportional chambers are installed. This allows for the tracking of the trajectory of charged particles. They cover the complete angle ϕ and an angle θ between 16° and 155°.

Barrel

The next layer consists of 5 mm thin plastic scintillators that form a barrel. Each one of these 32 segments covers an angle θ from 25° to 155° and together the whole angle ϕ. This barrel detector could help identify charged particles by combining the energy particles deposit in the barrel and the BGO when considering Bethe-Bloch. Unfortunately, the calibration of this detector is not completed and it will only be used to identify charged from uncharged particles in this thesis.

BGO

The last and main part of the central detectors is the BGO calorimeter. It consists of 480 bismuth germanium oxide (BGO) crystals and covers the whole range of ϕ in 32 sections and θ between 25° to 155° in 15 sections. Each crystal has a length of 24 cm which represents a radiation length of approximately $21X_0$. With this configuration, the kinetic energy and direction of particles can be

measured. The BGO is optimised for the detection of photons with its good energy resolution and small radiation length. The electromagnetic shower induced by high energetic photons creates light via scintillation, which is read out with photomultiplier tubes (PMT) behind each crystal.

4.2.3 Forward spectrometer

Particles that emerge from the reaction with an angle θ smaller than 12.1° and 8.2° in horizontal and vertical direction respectively [20] are detected by the forward spectrometer. An overview of this can be seen in figure 4.5.

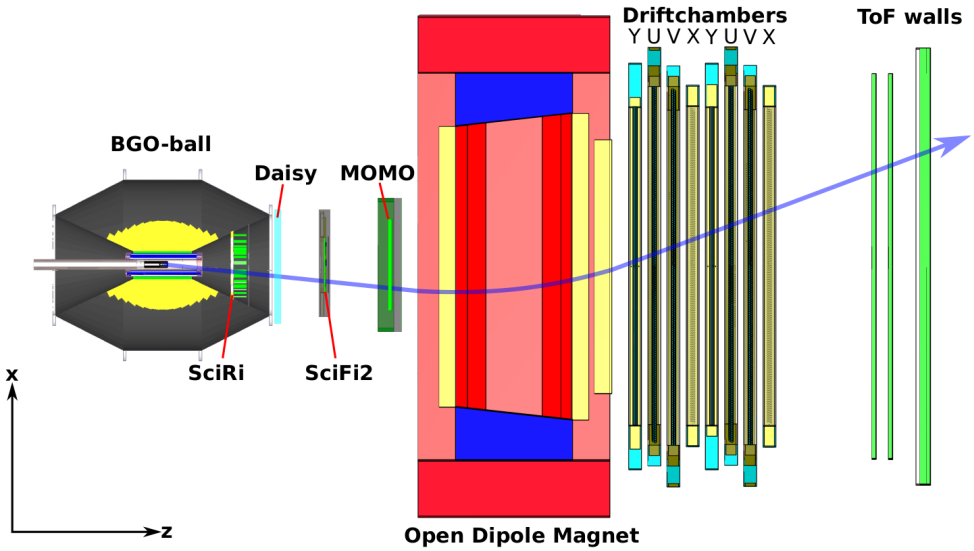

Figure 4.5: Top view of the BGO-OD experiment. The blue line shows the trajectory of a typical charged particle in the magnetic field of the open dipole magnet. The drift chamber 'Y' has the wires horizontally orientated, while the drift chamber 'X' has vertical orientation. Drift chambers 'U' and 'V' are rotated by ±9°relatively to the 'X' chamber [25].

To cover the remaining angular range between the central detectors and the forward spectrometer two additional systems are built in as intermediate detectors.
SciRi (**Sci**ntillating **Ri**ng) consists of 96 plastic scintillators divided into 32 segments for ϕ and three for θ. It covers the whole ϕ range and the region 10° to 25° in θ. The second detector Daisy is a multi-gap resistive plate chamber (MRPC) that is currently in commission.
Particles that reach the forward spectrometer will be detected by two detectors to determine their direction. After this, they pass through the open dipole magnet and get deflected depending on their charge and velocity. Then several drift chambers measure the trajectory after the deflection and the momentum of charged particles can be determined. Additionally, time-of-flight detectors are used for particle identification.

MOMO und SciFi2

The trajectory in front of the dipole magnet is measured by MOMO and SciFi2. Both of them are scintillating fiber detectors with strongly shielded PMTs against magnetic fields. They differ in the arrangement of their fibers. MOMO consists of rotated, overlapping modules and SciFi2 utilises a horizontal and vertical overlap of fibers.

Open Dipole Magnet

The main part of the forward spectrometer is the open dipole magnet. Its maximum integrated magnetic field at 1340 A is approximately 0.71 Tm [20].

Drift chambers

For the trajectory of particles behind the magnet eight drift chambers are used. These consist of two layers with drift cells in a hexagonal structure. To improve the track reconstruction, two of them are rotated by 90° and four of them by ±9° relative to the remaining two. This system provides a position resolution of $\delta x < 300$ μm and achieves a momentum resolution of 6% for magnetic fields at half maximum [20].

ToF

The **T**ime **o**f **F**light spectrometer consists of three walls with horizontal plastic scintillator bars. Each bar has two PMTs, that are at each end of the scintillator. For the horizontal position, the time difference measured by both PMTs is used. The vertical position of the hit corresponds to the position of the bar. By comparing the time information of the tagger the velocity β of the detected particle can be calculated. When combining multiple walls, a time resolution of $\sigma = 0.34$ ns is achieved [20]. The velocity of the particle can be combined with the measured momentum done by the detection systems explained before, to determine the mass of the particle. Figure 4.6 shows the distribution between the velocity β and the momentum of one charged particle in the forward spectrometer. The visible lines in this diagram represent different particles, which is further discussed in section 6.1.

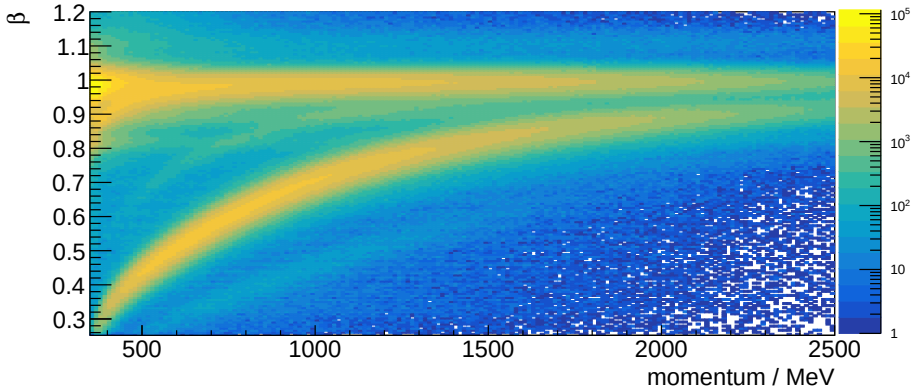

Figure 4.6: Velocity β against the momentum of charged particles in the forward spectrometer. The colour depicts the number of entries.

4.2.4 Photon flux

At the end of the experimental setup, the photon flux is monitored. This is done by the **G**amma **I**ntensity **M**onitor (GIM) and the **Flu**x **Mo**nitor (FluMo).
GIM is a fully absorbing glass lead detector. Its use is limited by radiation damage and the high photon rates that are used during data taking. Due to its high accuracy, it is used for the calibration of FluMo. FluMo consists of five plastic scintillators and indirectly measures the photon flux through detection of electron-positron pairs.

CHAPTER 5

Analysis tools

In this chapter, two important tools used in this analysis will be discussed. The kinematic fit in section 5.1 is used to optimise the resolution of the measured data and RooFit in section 5.2 for signal and background separation. This chapter only gives an overview of these techniques for a better understanding of the analysis in chapter 6. A more detailed description of these tools can be found in Ref. [25].

5.1 Kinematic Fit

Kinematic fitting is a software technique for optimizing the resolution of the experimentally obtained data. It takes the initially measured parameters and varies them within their errors with respect to momentum and energy conservation as constraints. This method was implemented in the BGOOD software framework ExPLORA by Georg Scheluchin [25]. Detailed information about kinematic fitting can be found in Ref. [26] and Ref. [27].
The representation of the three momenta p_x, p_y, p_z, the energy E of a particle and the coordinates of the reaction vertex will be defined as a tack. All parameters of n tracks will be represented by the vector α:

$$\alpha = \begin{pmatrix} \alpha_1 \\ \alpha_2 \\ \vdots \\ \alpha_n \end{pmatrix} \tag{5.1}$$

The vector α_A holds all initially measured parameters, whereas α_0 holds the initial parameters for one iteration of fitting. The constraints will be defined as $H(\alpha) = 0$. With a Taylor expansion around the point α_A they will be written as

$$0 = \left(\frac{\partial H(\alpha_A)}{\partial \alpha} \right) (\alpha - \alpha_A) + H(\alpha_A) = D\delta\alpha + d \tag{5.2}$$

with $\delta = \alpha - \alpha_A$,

$$D = \begin{pmatrix} \frac{\partial H_1}{\partial \alpha_1} & \frac{\partial H_1}{\partial \alpha_2} & \cdots & \frac{\partial H_1}{\partial \alpha_n} \\ \frac{\partial H_2}{\partial \alpha_1} & \frac{\partial H_2}{\partial \alpha_2} & \cdots & \frac{\partial H_2}{\partial \alpha_n} \\ \vdots & \vdots & \ddots & \vdots \\ \frac{\partial H_n}{\partial \alpha_1} & \frac{\partial H_n}{\partial \alpha_2} & \cdots & \frac{\partial H_2}{\partial \alpha_n} \end{pmatrix} \tag{5.3}$$

and

$$d = \begin{pmatrix} H_1(\alpha_A) \\ H_2(\alpha_A) \\ \vdots \\ H_r(\alpha_A) \end{pmatrix} \tag{5.4}$$

These constraints can then be used for the method of Lagrange multipliers, where the function χ^2 is minimised

$$\chi^2 = (\alpha - \alpha_0)^T V_{\alpha_0}^{-1} (\alpha - \alpha_0) + 2\lambda^T (D\delta\alpha + d) \tag{5.5}$$

with respect to α and the Lagrange multiplier λ. Here $V_{\alpha_0}^{-1}$ is the covariance matrix defined by $cov(x_i, x_j) \equiv V_{x\,ij} = \langle (x_i - \bar{x_j})(x_j - \bar{x_j}) \rangle \equiv \langle \delta x_i \delta x_j \rangle$. This yields the result:

$$\alpha = \alpha_0 - V_{\alpha_0} D^T \lambda \tag{5.6}$$

$$\lambda = V_D (D\delta\alpha_0 + d) \tag{5.7}$$

$$V_D = (D V_{\alpha_0} D^T)^{-1} \tag{5.8}$$

$$V_\alpha = V_{\alpha_0} - V_{\alpha_0} D^T V_D D V_{\alpha_0} \tag{5.9}$$

$$\rightarrow \chi^2 = \lambda^T V_D^{-1} \lambda = \lambda^T (D\delta\alpha_0 + d) \tag{5.10}$$

With this, the constraints and initial parameters can be inserted and the fitted values with given iterations calculated. Furthermore, the deviation of the new values to the original one can be described by a pull function and χ^2 converted to a confidence level, which indicates the probability for the new value to be right. For more information on this and examples Ref. [25] is suggested.

5.2 RooFit

RooFit is a toolkit for data modeling integrated in ROOT [28]. It uses a maximum likelihood method and allows for an easy graphical representation. This thesis utilises RooFit to separate the background from the signal. For this, Monte Carlo simulations for the expected signal and background reaction channels are made. This simulation is attuned to the spatial, energy and time resolution of the experiment for the results to be consistent with the real data. The results depend strongly on the precision of the simulated geometry. For a better illustration of the RooFit figure 5.1 can be viewed.

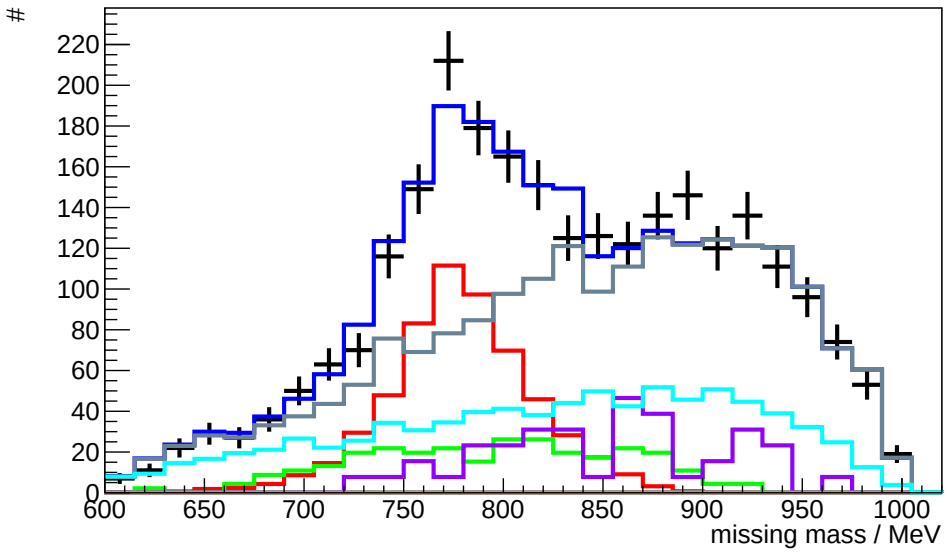

Figure 5.1: Distribution of the missing mass to the proton for the reaction $\gamma p \rightarrow \omega p$ with RooFit. The black data points are real data, the red line is the simulated signal, the grey line is the summed background and the blue line is the background and signal combined. The background consists of the green line for the $K^0\Sigma^+$ channel, the cyan line for the $\pi^+\pi^-\pi^0 p$ channel and the purple line for the $K^+\Sigma^0$ channel.

The red signal line together with all simulated background channels are scaled in a way that the sum of all (blue line) matches the black data points. In this example, only the most relevant background channels are shown.

CHAPTER 6

Reconstruction of the $\gamma p \rightarrow \omega p$ reaction channel

This chapter goes over the different steps in the reconstruction of the $\gamma p \rightarrow \omega p$ reaction. First, section 6.1 presents the selection of the proton in the forward spectrometer. In section 6.2 the decay channels and the corresponding event selections are discussed. Finally, in section 6.3 the background subtraction and yield extraction are shown.
The data viewed in this chapter is taken from the beamtime in April 2017. This three weeks long running period collected data with a rate around $2.5 \cdot 10^7$ s^{-1} tagged photons [20].

6.1 Proton selection

This thesis focuses on the backward production of ω mesons which requires protons to be found at forward angles in the center of mass frame. Therefore only events with protons in the forward spectrometer are considered. At first, all events are filtered for those with at least one charged particle in the forward spectrometer. These kinds of event selections by excluding data that do not fulfil a condition is referred to as a cut. The distribution between the velocity β and the momentum of charged particles in the forward spectrometer can be seen in figure 6.1. The visible ridges in this diagram

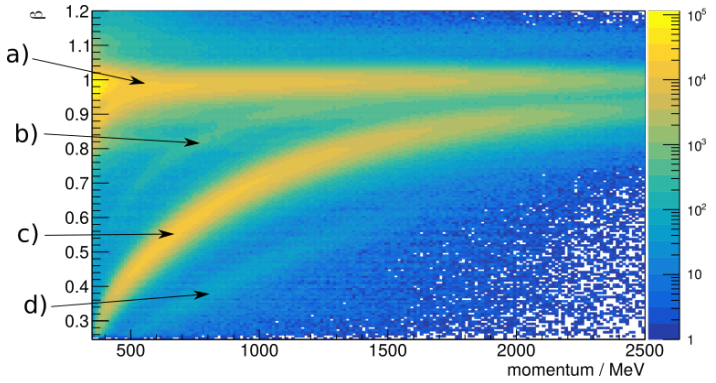

Figure 6.1: Velocity β against the momentum of charged particles in the forward spectrometer. Line a) represents electrons and pions, line b) shows kaons, line c) corresponds to protons and line d) to deuterons. The colour depicts the number of entries.

represent different particles. The horizontal line a) corresponds to electrons and pions. The next line

b) shows kaons, followed by c) for protons and d) for deuterons. To ensure that the charged particle is a proton, the mass calculated by the combination of the measured velocity β and momentum of the particles is used. This mass will be referred to as ToF mass. Figure 6.2 shows the distribution of the determined ToF mass for the required charged particle. The peak around the proton mass

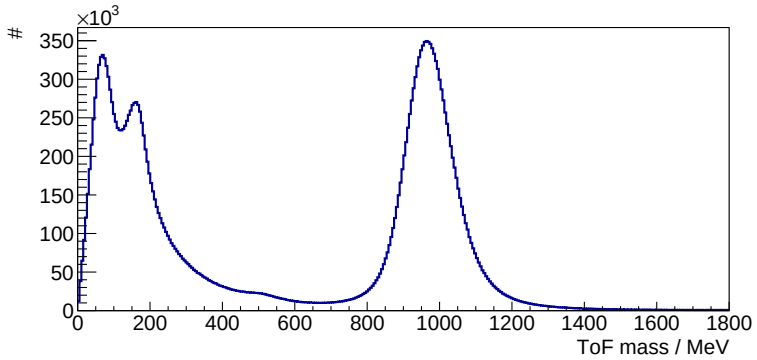

Figure 6.2: Distribution of the ToF mass, calculated from the velocity and momentum of the particle required in the forward spectrometer.

$m_p \approx 938$ MeV [2] is clearly visible and a cut of 3σ is applied. The remaining events are depicted in figure 6.3. This shows only the desired proton line. The mass of the selected particles is fixed to the

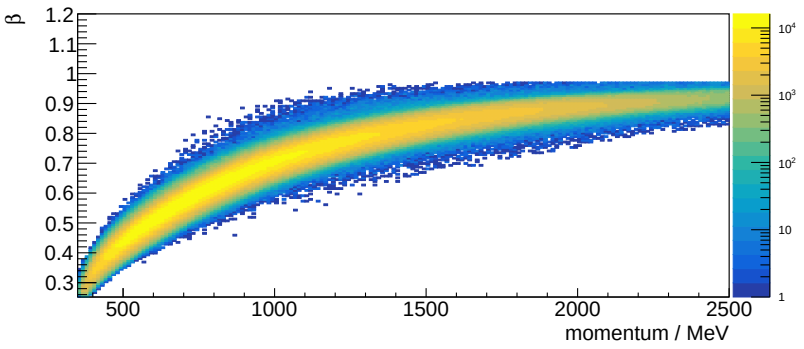

Figure 6.3: Velocity β against the momentum of the charged particle required in the forward spectrometer after the cut to the ToF mass. The colour depicts the number of entries.

proton mass of $m_p \approx 938$ MeV [2] for the following analysis.

6.2 Selection of the reaction channel

After identifying the proton the missing mass (shown in section 2.2) can be used to determine the other particle in the final state. In figure 6.4 the missing mass is shown. The distribution contains

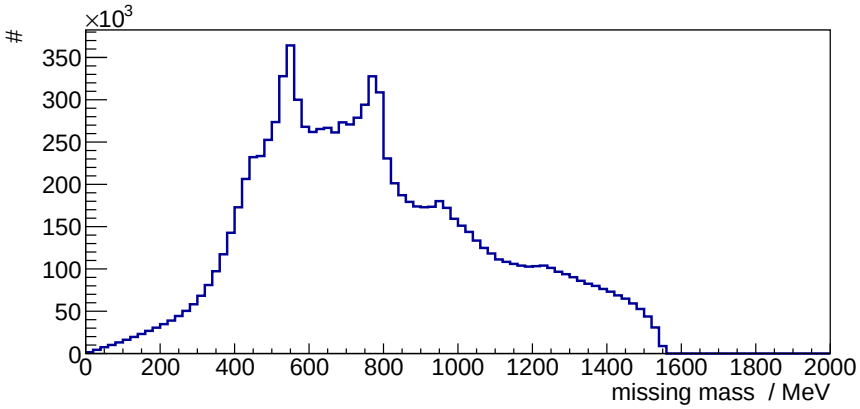

Figure 6.4: Distribution of the missing mass to the proton in the forward spectrometer

non-resonant contributions originating from three or more body reactions and peaks corresponding to the mass of different neutral mesons from two body reactions. The reactions $\gamma p \rightarrow \eta p$ with $m_\eta \approx 548$ MeV [2], $\gamma p \rightarrow \omega p$ with $m_\omega \approx 783$ MeV [2] and $\gamma p \rightarrow \eta' p$ with $m_{\eta'} \approx 958$ MeV [2] are easy to spot. The $\gamma p \rightarrow \rho^0 p$ reaction contributes a broad enhancement around its mass of $m_\rho \approx 775$ MeV [2].

To improve the signal-to-background ratio for the ω meson peak additional cuts that enhance the expected signature of the ω decays are needed. To find the optimal cut, which balances the gain in signal-to-background ratio with the possible losses in statistics, several selection cuts were considered for this analysis. These were separated into both decay channels discussed in section 2.1 and require different numbers of particles detected additionally to the proton. Starting from cuts with no additional particles to the proton up to exactly all expected particles with the right charge required were taken into account. The best results were found for both decay channels in the case of full reconstruction. For the $\omega \rightarrow \pi^0\gamma \rightarrow \gamma\gamma\gamma$ channel three neutral particles and for the $\omega \rightarrow \pi^+\pi^-\pi^0 \rightarrow \pi^+\pi^-\gamma\gamma$ channel two charged and two uncharged particles needed to be detected. Furthermore, a cut that selects initial photon energies above ω threshold of $E_\gamma > 1109$ MeV is applied.

In figure 6.5(a) the distribution of the missing mass to the proton for the $\pi^0\gamma$ channel can be seen. This shows the ω peak with much background beneath it. This can be improved with a kinematic fit with π^0-mass constraint. The resulting distribution can be seen in figure 6.5(b) and shows a good signal-to-background ratio.

For the $\pi^+\pi^-\pi^0$ channel the distribution of the missing mass is depicted in figure 6.6(a). It shows the ω peak and for higher missing masses the η' peak, since the $\eta' p$ reaction may decay into the same final state particles. Similar to the neutral decay channel a kinematic fit with π^0-mass constraint is applied to improve the signal-to-background ratio in figure 6.6(b).

Since further analysis requires high statistics the $\pi^+\pi^-\pi^0$ channel is used due to the much higher branching ratio seen in section 2.1. The neutral channel with its good signal-to-background ratio might be a good candidate for future analysis with more combined beamtime data.

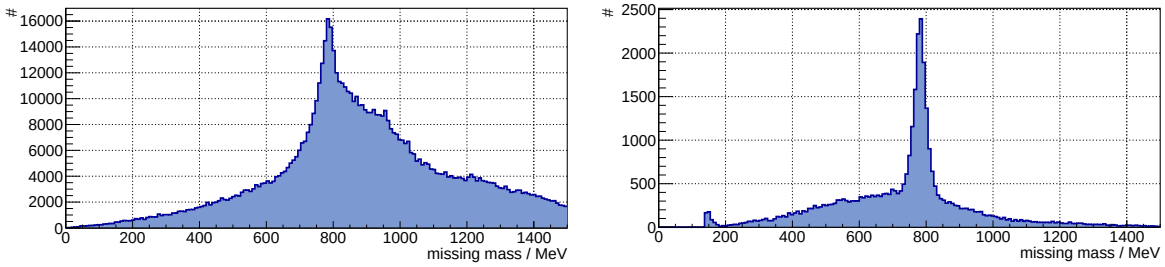

(a) without kinematic fit (b) with kinematic fit

Figure 6.5: Distribution of the missing mass to the proton in the forward spectrometer for the $\pi^0\gamma$ channel a) and with an additional kinematic fit b)

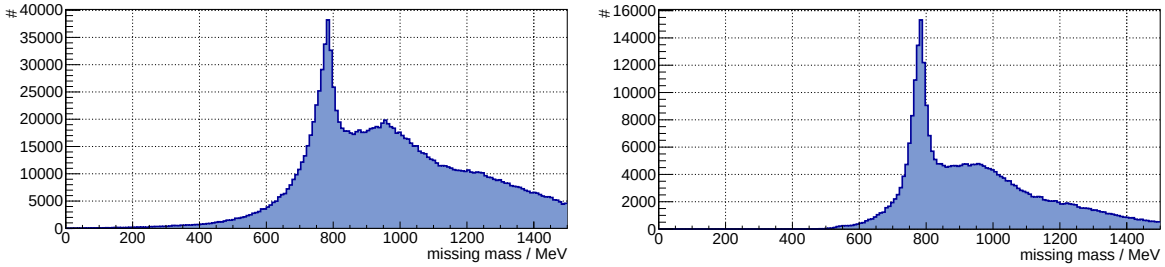

(a) without kinematic fit (b) with kinematic fit

Figure 6.6: Distribution of the missing mass to the proton in the forward spectrometer for the $\pi^+\pi^-\pi^0$ channel a) and with an additional kinematic fit b)

The data used in the following combine the proton selection cut, the full reconstruction cut of the $\pi^+\pi^-\pi^0$ channel, the ω production threshold cut and the kinematic fit.
For the determination of the differential cross section the data are divided into $\cos(\theta_{\mathrm{CMS}})$ and photon energy E_γ intervals, referred to as bins. The analysis uses the photon energy range 1109 MeV < E_γ < 1959 MeV with 50 MeV steps and the angular range $-0.99 < \cos(\theta_{\mathrm{CMS}}) < -0.9$ with steps of 0.03.

6.3 Yield extraction

In each energy and angle bin, it is necessary to separate signal from background and extract the signal yield. To demonstrate this two example regions are illustrated here. Figure 6.7 shows the missing mass distribution for two different energy and θ_{CMS} angles. In the left figure 6.7(a) a peak around the ω mass with some background underneath can be seen. For higher energies this background extents to higher missing masses, but the ω peak is still visible as shown in figure 6.7(b). To differentiate

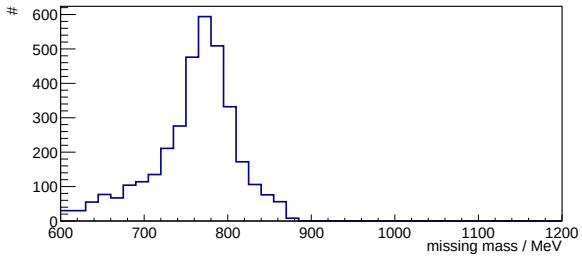

(a) Distribution of the missing mass to the proton for 1259 MeV < E_γ < 1309 MeV and −0.99 < cos(θ_{CMS}) < −0.96.

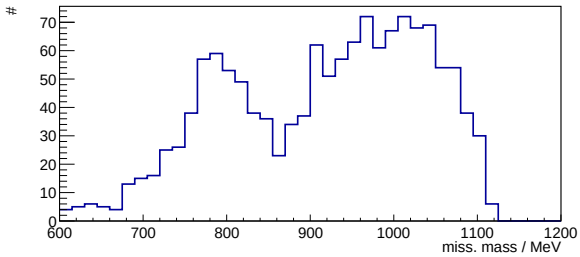

(b) Distribution of the missing mass to the proton for 1759 MeV < E_γ < 1809 MeV and −0.96 < cos(θ_{CMS}) < −0.93

Figure 6.7: Distribution of the missing mass to the proton for two different energies and θ_{CMS} angles

between signal and background, RooFit, which is described in section 5.2, is used. For this the signal channel and several background channels were simulated. Channels that decay into the same final state and even channels with an extra particle or one particle less than the expected final state were considered, since particles can be undetected or misinterpreted. These background channels include $\pi^+\pi^-\pi^0 p$, $\mathrm{K}^0\Sigma^+$, $\mathrm{K}^+\Lambda^0$, $\mathrm{K}^+\Sigma^0$, $\eta'\mathrm{p}$ and $\mathrm{K}^+\Sigma^+\pi^-$. To all simulations the same cuts as for the real data were applied. The results of these RooFits can be found in figure 6.8. Here the background contains

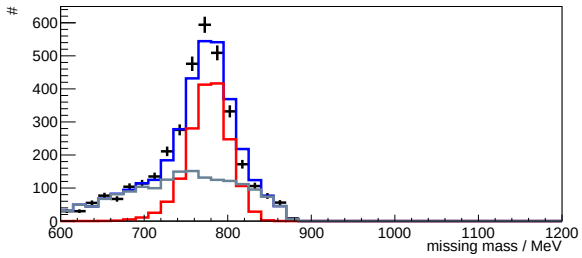

(a) Distribution of the missing mass to the proton with RooFit for 1259 MeV < E_γ < 1309 MeV and −0.99 < cos(θ_{CMS}) < −0.96

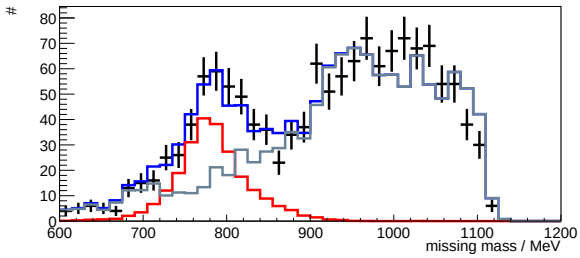

(b) Distribution of the missing mass to the proton with RooFit for 1759 MeV < E_γ < 1809 MeV and −0.96 < cos(θ_{CMS}) < −0.93

Figure 6.8: Distribution of the missing mass to the proton with RooFit for two different energies and θ_{CMS} angles. The black data points are real data, the red line is the simulated signal, the grey line is the summed background and the blue line is the background and signal combined.

multiple channels, but only the sum of them is shown for a better illustration. In figure 6.9 the most dominant channels for this fit are also displayed to better understand the fit. In most energy and angle bins the uncorrelated production of $\pi^+\pi^-\pi^0 p$ contributes significantly to the background. Further

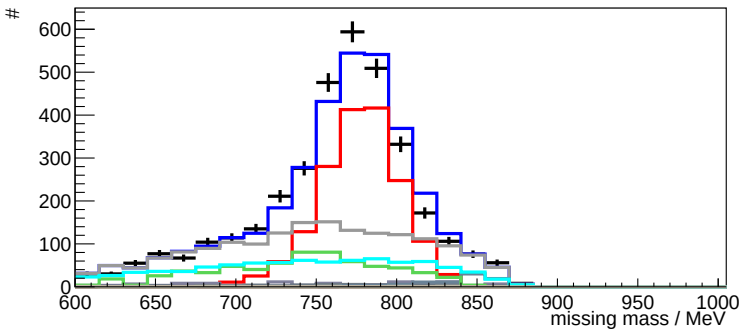

Figure 6.9: Distribution of the missing mass to the proton with RooFit for photon energies 1259 MeV < E_γ < 1309 MeV and angles $-0.99 < \cos(\theta_{\mathrm{CMS}}) < -0.96$. The black data points are real data, the red line is the simulated signal, the grey line is the summed background and the blue line is the background and signal combined. The most dominant channels of the background are the green line for the $K^0\Sigma^+$ channel and the cyan line for the $\pi^+\pi^-\pi^0 p$ channel.

channels which affect the shape of the background in most bins are $K^0\Sigma^+$, $K^+\Lambda^0$ and $K^+\Sigma^0$. For higher energies, the background seen for higher missing masses includes the $\eta' p$ and $K^+\Sigma^+\pi^-$ channels.
The yield of the ω channel can now be extracted from the fitted signal (red line) of the fit.
To cross-check this extraction, the yield was determined by a second method. This extraction uses a simple polynomial of second order to fit the background. The fit excluded the data within 3σ of the peak. The yield can then be taken from the difference between the complete integral and the integral of the fit function. Figure 6.10 displays the same region as shown in figure 6.9 with the cross-check method. For this bin, both methods yield similar results. For a better comparison figure 6.11 illustrates

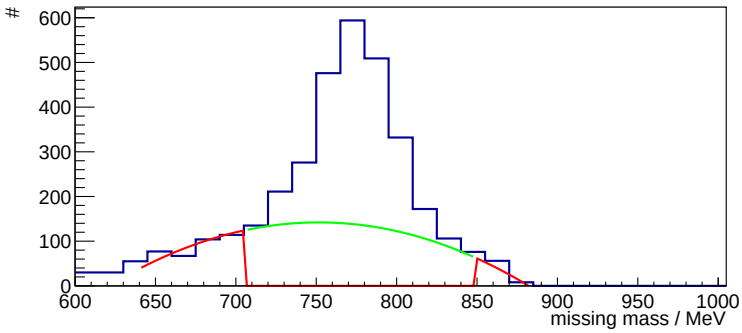

Figure 6.10: Distribution of the missing mass to the proton for photon energies 1259 MeV < E_γ < 1309 MeV and angles $-0.99 < \cos(\theta_{\mathrm{CMS}}) < -0.96$. Additionally, a polynomial of second order is fitted to it with the peak region excluded. The fit function is shown in red with extrapolation in green for the excluded region.

the ratio $\frac{N_{\mathrm{cross}}}{N_{\mathrm{roofit}}}$ between the yield of the cross-check method and the yield of the RooFit method for different photon energies. The polynomial fit was not designed to cover all energy and angle regions. Therefore it only gives reasonable results for energies below E_γ < 1359 MeV. In higher energy bins, the background for higher missing masses prevents the cross-check method from working. In the energy region presented in figure 6.11, the yields of both methods are in agreement.
For the analysis of the differential cross section in the next chapter, the RooFit yield was used.

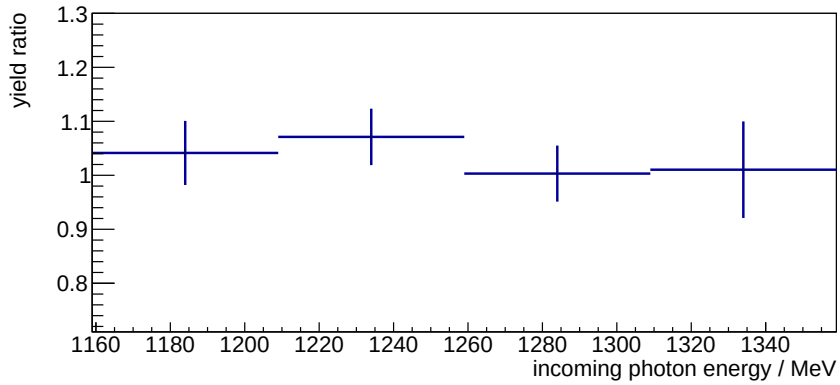

Figure 6.11: Ratio of the yields from both methods depending on the photon energy E_γ for angles of $-0.99 < \cos(\theta_{\mathrm{CMS}}) < -0.96$. The ratio is formed by the yield of the polynomial fit divided by the yield of the RooFit.

CHAPTER 7

Differential cross section of the $\gamma p \rightarrow \omega p$ reaction channel

In this chapter, the analysis for the differential cross section of the $\gamma p \rightarrow \omega p$ reaction channel will be presented. Furthermore, the results will be compared to data from experiments mentioned in chapter 3. The differential cross section $\frac{d\sigma}{d\Omega}$ is be determined by

$$\frac{d\sigma}{d\Omega}(E_\gamma, \theta) = \frac{1}{n \cdot z} \cdot \frac{1}{\Omega} \cdot \frac{1}{F(E_\gamma)} \cdot \frac{1}{\epsilon(E_\gamma, \theta)} \cdot N(E_\gamma, \theta) \tag{7.1}$$

Here the first fraction contains the area density $A = n \cdot z$ which combines the target density n and the target cell length z. For the 2017 beamtime with liquid hydrogen, the area density was determined to be $A = (2.59 \pm 0.04) \cdot 10^{-7} \mu b^{-1}$ [25].
The next factor is the solid angle $\Omega = \int \sin(\theta_{\text{CMS}}) \mathrm{d}\theta_{\text{CMS}} \mathrm{d}\phi$. Since this analysis covers the complete angular range of ϕ, the solid angle can be written as $\Omega = 2\pi \cdot (\cos(\theta^1_{\text{CMS}}) - \cos(\theta^2_{\text{CMS}}))$. This includes the size of the angular regions and can therefore be fixed to $\Omega = 2\pi \cdot 0.03$ in this analysis.
To normalise the reconstructed events, the photon flux $F(E_\gamma)$ in section 7.1 needs to be considered. It is the number of photons for which the reaction could have occurred and dependents on the initial photon energy.
The next part is the detection efficiency $\epsilon = \frac{N^{\text{detec}}_{\text{sim}}}{N^{\text{total}}_{\text{sim}}}$. This is determined in section 7.2 by the total number of simulated signal reactions $N^{\text{total}}_{\text{sim}}$ and the number of reconstructed reactions by the analysis $N^{\text{detec}}_{\text{sim}}$.
Finally, the yield for the specific energy and angle bin $N(E_\gamma, \theta)$ described in the previous chapter is used.

7.1 Photon flux

The photon flux is the distribution of incident photon energies measured by GIM and FluMo described in section 4.2 and can be seen in figure 7.1(a). The process of incoherent bremsstrahlung shapes these counts proportional to $\frac{1}{E_\gamma}$. Additionally this distribution shows some jumps, that originate from the changing bin width. Figure 7.1(b) shows the photon flux with each bin divided by its bin

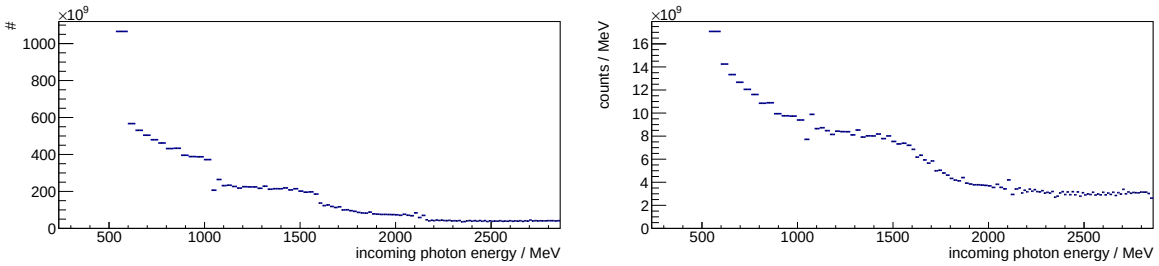

(a) without normalisation

(b) with normalisation by bin width

Figure 7.1: Distribution of incident photon energy a) and with normalisation b)

width. Furthermore an increase between $E_\gamma = 1200$ MeV and $E_\gamma = 1800$ MeV can be seen. This is caused by the coherent bremsstrahlung process, due to the use of a diamond radiator. This beamtime is composed of data with two linear polarisations orthogonal to each other. Since the sum of this beamtime data contains both orientations equally often, it results in unpolarised data if added together. For this analysis, the photon flux is binned accordingly to the energy bin width described in chapter 6. This distribution is depicted in figure 7.2

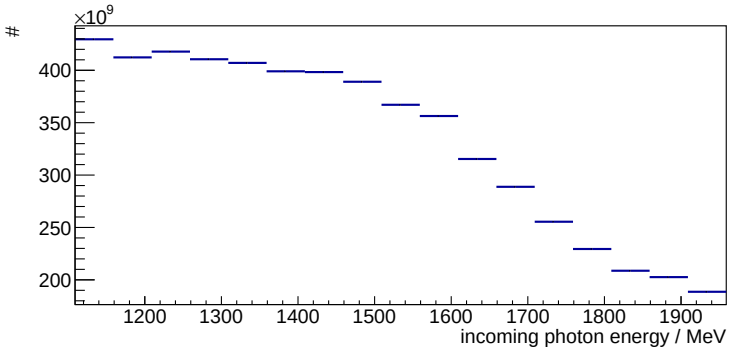

Figure 7.2: Distribution of incident photon energy with bin sizes of 50 MeV.

7.2 Detection efficiency

The detection efficiency $\epsilon = \frac{N_{\text{sim}}^{\text{detec}}}{N_{\text{sim}}^{\text{total}}}$ is determined based on simulated data. For this, the $\gamma p \rightarrow \omega p$ channel is simulated and the reconstruction cuts which were used for the real data are applied. Then for each energy and angle bin, the quotient of the reconstructed reactions and all generated reactions is calculated. An overview of this can be seen in figure 7.3. The visible shape of this distribution corresponds to the acceptance of the forward spectrometer.
In the angular region $-0.93 < \cos(\theta_{\text{CMS}}) < -0.9$ the detection efficiency ϵ shows a maximum right after threshold and decreases with higher photon energies. This is caused by the upper limit in polar angle θ_{lab} of the proton to be detected in the forward spectrometer. With higher energies, the protons are more likely to exceed this limit.
For more forward angles θ_{CMS} of the proton in center of mass frame, this effect is reduced. Additionally

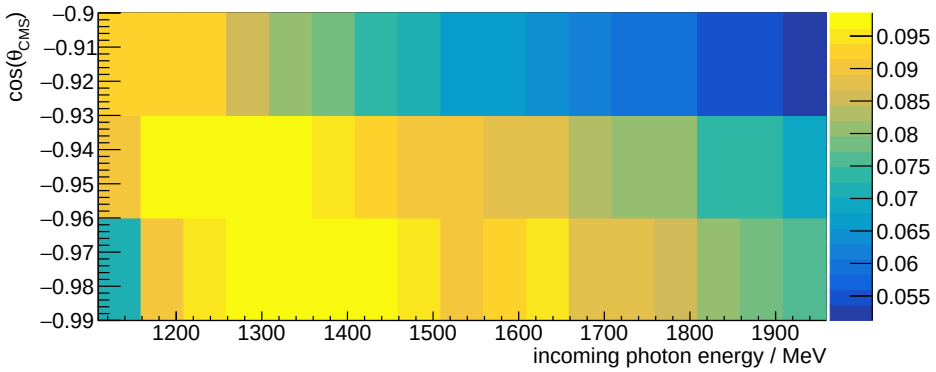

Figure 7.3: Simulated detection efficiency for the different $\cos(\theta_{\mathrm{CMS}})$ and photon energy E_γ regions. The colour indicates the detection efficiency.

at most forward angles of the proton near threshold the lower limit of the forward spectrometer can be observed. In this kinematic region, the proton is likely to stay near the beamline and will not be detected.

7.3 Systematic errors

There are systematic uncertainties that affect the extraction of the differential cross section. Some of them are known and can be roughly estimated. Table 7.1 lists these errors with an overall systematic error summed in quadrature of 11%. The target size depends on the exact beam position and on the

Description	systematic error in %
target size	2
photon flux number	5
kinematic fit	4
Monte Carlo Simulation	9
RooFit	2
overall systematic error	11

Table 7.1: All known systematic errors listed with an overall systematic error summed in quadrature. Each error is only estimated.

curvature of the Mylar windows around the target cell. The systematic error of the photon flux is linked to the efficiency of FluMo. Both the kinematic fit and the Monte Carlo Simulation depend strongly on the precision of the detector geometry in the simulation. For RooFit a simulated channel not represented in the real data can cause systematic errors. All systematic errors are only estimated and no intensive study has been carried out.

7.4 Results

All parameters are inserted into equation 7.1 to obtain the differential cross section of the $\gamma p \rightarrow \omega p$ reaction channel. Figure 7.4 displays the differential cross section against the photon energy E_γ for all angular regions. In all three the cross section starts to increase after threshold and reaches a peak at around $E_\gamma \approx 1280$ MeV. Afterwards, it decreases slowly with higher energies. The peak is more pronounced at most backward θ_{CMS} angles, corresponding to most forward going protons in the laboratory system. In the higher energy region, the data points stay mostly at the same height for different angles.
When comparing the data of this analysis to other experiments mostly overall agreement can be observed. In the energy region 1109 MeV < E_γ < 1409 MeV Crystal Ball data show a more flat distribution with lower differential cross section values. CBELSA 2015 data in this energy region lies between Crystal Ball and the data of this analysis.
For photon energies above $E_\gamma \approx 1500$ MeV LEPS data and the data of this thesis agree, while CBELSA 2015 lies slightly higher.
Figure 7.5 displays the differential cross section against $\cos(\theta_{\text{CMS}})$ for the two example energy regions seen in section 3.6. In figure 7.5(a) the data of this analysis shows a strong backward enhancement, which is not present in the data of other experiments. Only the most backward data point of CBELSA 2015 suggest a higher differential cross section value towards backwards angles.
Figure 7.5(b) further shows the agreement between LEPS data and this analysis. Both depict a decrease in differential cross section towards more backward angles, which agrees to CLAS data.
Figure 7.6 and figure 7.7 give a complete overview of the differential cross section against $\cos(\theta_{\text{CMS}})$. Overall in the lower energy region E_γ < 1450 MeV the data points of this analysis lie above most other experiments. This strong increase of differential cross section towards more backward angles might imply strong u-channel contributions. For higher energies, the data points of this analysis show similar values or lie slightly below most other experiments, with overall agreement especially to LEPS data. The cause of the discrepancy with other experiments for low energies could not yet be identified and future studies are needed.

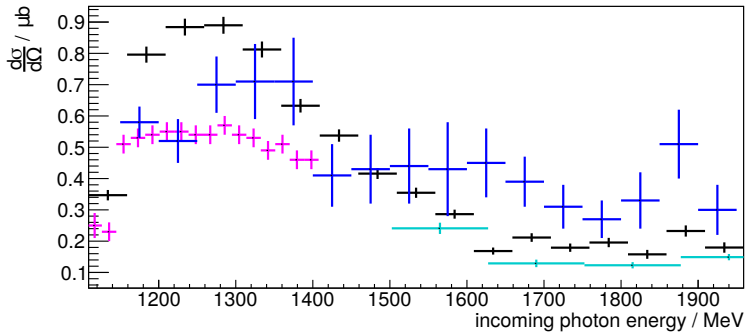

(a) Differential cross section against incident photon energy E_γ with the ω meson at $-0.99 < \cos(\theta_{\mathrm{CMS}}) < -0.96$. In black the data of this analysis, in red/blue CBELSA 2014/2015 [10] [11] data, in magenta Crystal Ball [12] data and in cyan LEPS [13] data.

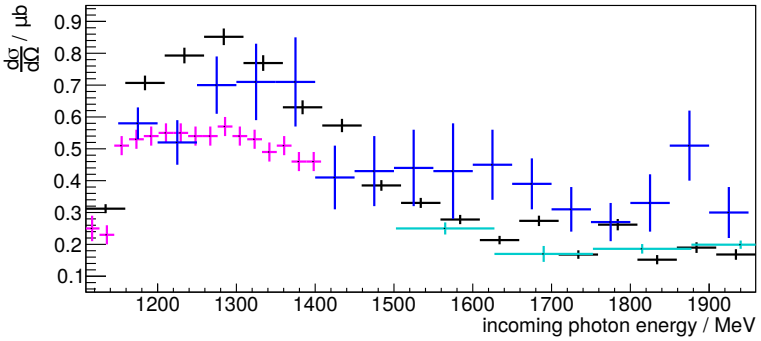

(b) Differential cross section against incident photon energy E_γ with the ω meson at $-0.96 < \cos(\theta_{\mathrm{CMS}}) < -0.93$. In black the data of this analysis, in red/blue CBELSA 2014/2015 [10] [11] data, in magenta Crystal Ball [12] data and in cyan LEPS [13] data.

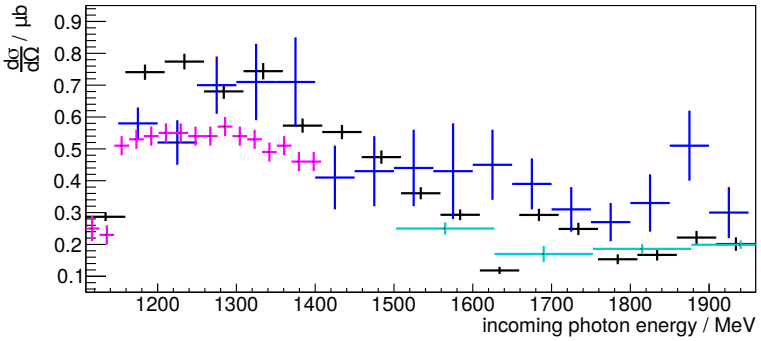

(c) Differential cross section against incident photon energy E_γ with the ω meson at $-0.93 < \cos(\theta_{\mathrm{CMS}}) < -0.9$. In black the data of this analysis, in red/blue CBELSA 2014/2015 [10] [11] data, in magenta Crystal Ball [12] data and in cyan LEPS [13] data.

Figure 7.4: Differential cross section $\frac{d\sigma}{d\Omega}$ against incident photon energy E_γ in the angular range of the ω meson $-0.99 < \cos(\theta_{\mathrm{CMS}}) < -0.9$ and data from other experiments.

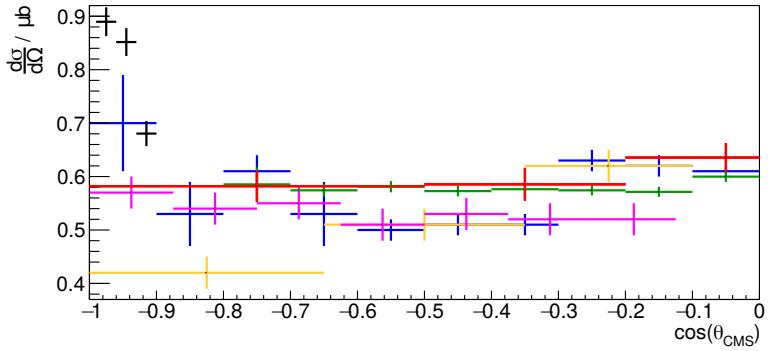

(a) Differential cross section $\frac{d\sigma}{d\Omega}$ against $\cos(\theta_{\mathrm{CMS}})$ of the ω meson in the incident photon energy range 1259 MeV < E_γ < 1309 MeV. In black the data of this analysis, in red/blue CBELSA 2014/2015 [10] [11] data, in green CLAS [8] data, in magenta Crystal Ball [12] data and in yellow SAPHIR [5] data.

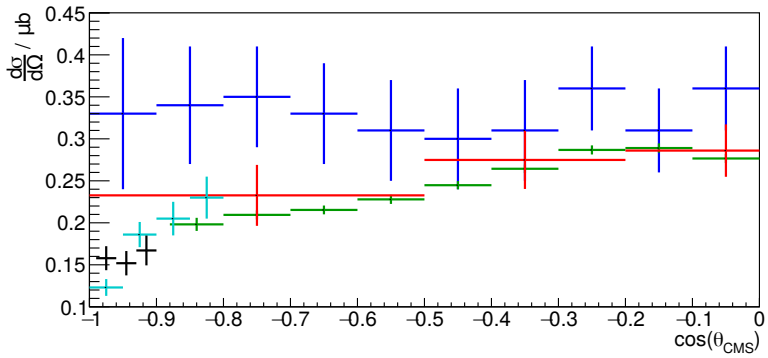

(b) Differential cross section $\frac{d\sigma}{d\Omega}$ against $\cos(\theta_{\mathrm{CMS}})$ of the ω meson in the incident photon energy range 1809 MeV < E_γ < 1859 MeV. In black the data of this analysis, in red/blue CBELSA 2014/2015 [10] [11] data, in green CLAS [8] data and in cyan LEPS [13] data.

Figure 7.5: Differential cross section $\frac{d\sigma}{d\Omega}$ against $\cos(\theta_{\mathrm{CMS}})$ of the ω meson for two different incident photon energy regions E_γ and data from other experiments.

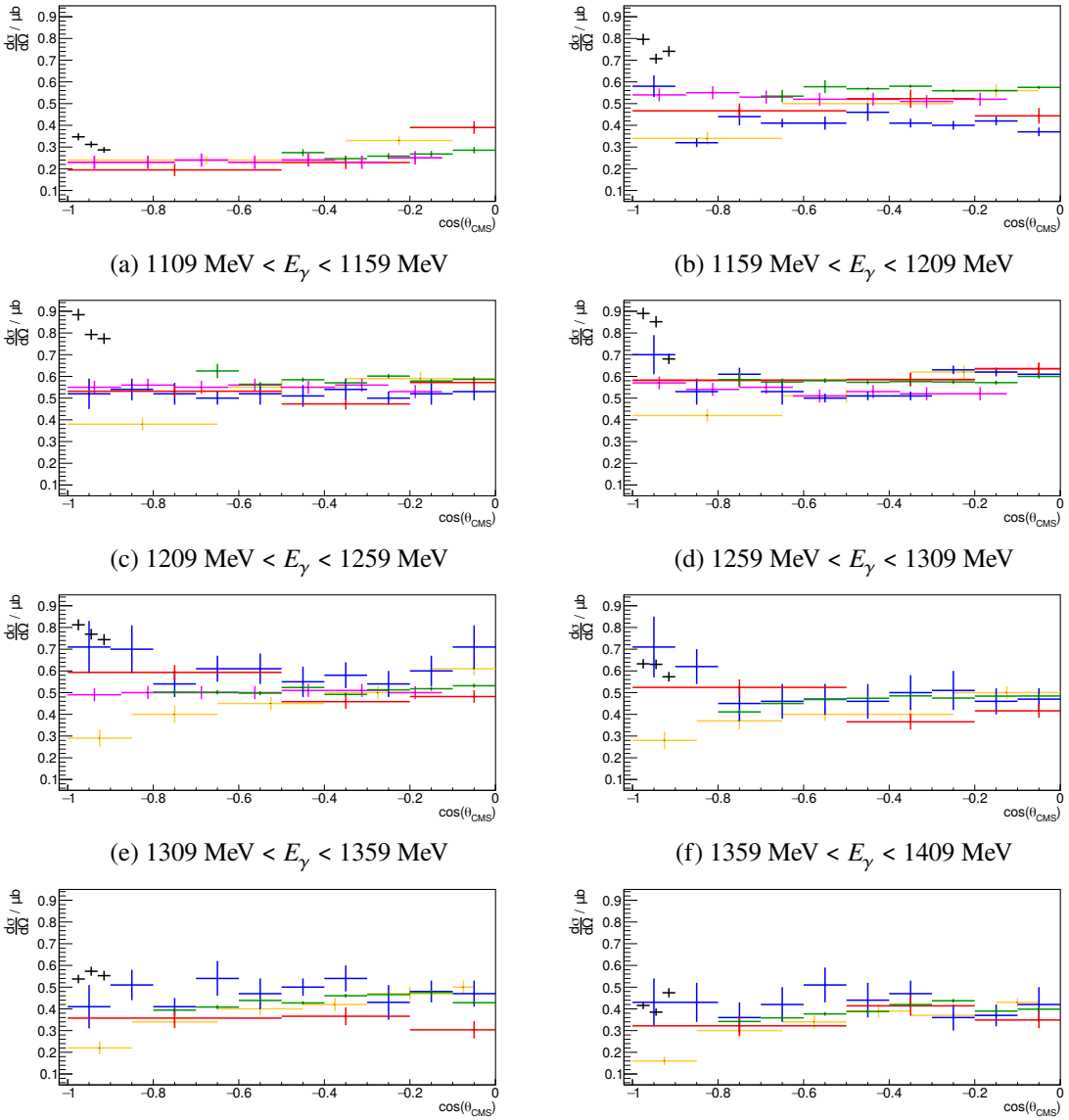

(a) 1109 MeV < E_γ < 1159 MeV

(b) 1159 MeV < E_γ < 1209 MeV

(c) 1209 MeV < E_γ < 1259 MeV

(d) 1259 MeV < E_γ < 1309 MeV

(e) 1309 MeV < E_γ < 1359 MeV

(f) 1359 MeV < E_γ < 1409 MeV

(g) 1409 MeV < E_γ < 1459 MeV

(h) 1459 MeV < E_γ < 1509 MeV

Figure 7.6: Differential cross section $\frac{d\sigma}{d\Omega}$ against $\cos(\theta_{\text{CMS}})$ of the ω meson for different E_γ. In black the data of this analysis, in red/blue CBELSA 2014/2015 [10] [11] data, in green CLAS [8] data, in magenta Crystal Ball [12] data, in yellow SAPHIR [5] data and in cyan LEPS [13] data.

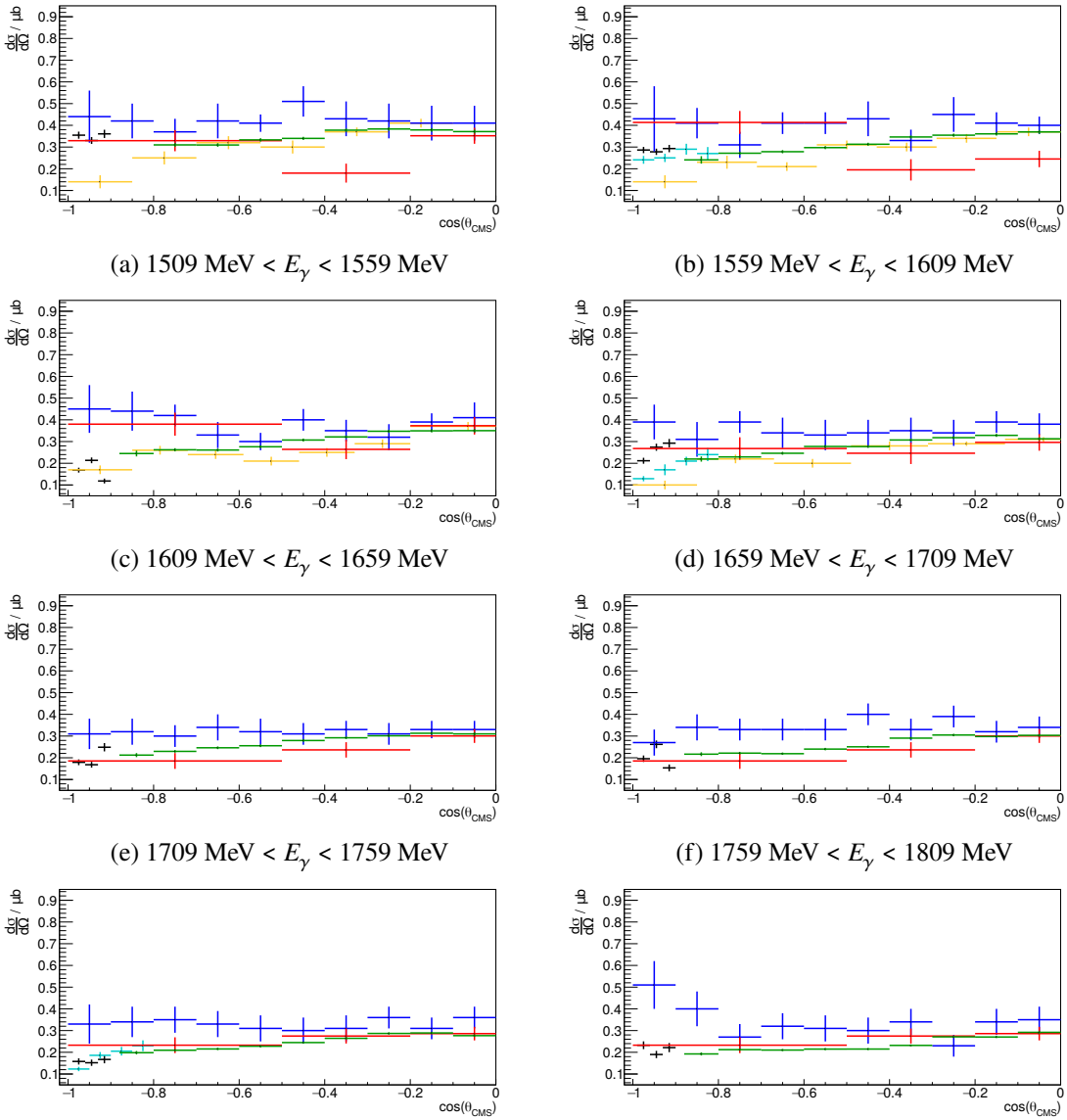

(a) 1509 MeV < E_γ < 1559 MeV

(b) 1559 MeV < E_γ < 1609 MeV

(c) 1609 MeV < E_γ < 1659 MeV

(d) 1659 MeV < E_γ < 1709 MeV

(e) 1709 MeV < E_γ < 1759 MeV

(f) 1759 MeV < E_γ < 1809 MeV

(g) 1809 MeV < E_γ < 1859 MeV

(h) 1859 MeV < E_γ < 1909 MeV

Figure 7.7: Differential cross section $\frac{d\sigma}{d\Omega}$ against $\cos(\theta_{\text{CMS}})$ of the ω meson for different E_γ. In black the data of this analysis, in red/blue CBELSA 2014/2015 [10] [11] data, in green CLAS [8] data, in magenta Crystal Ball [12] data, in yellow SAPHIR [5] data and in cyan LEPS [13] data.

CHAPTER 8

Summary and outlook

For the search of missing resonances, experiments worldwide explore the excitation of hadronic states in non-pionic channels with photoproduction. The $\gamma p \rightarrow \omega p$ reaction channel is well suited for this endeavour. Published data for this reaction revealed different contributions of reaction mechanisms. With high energies, the dominant contribution is diffractive scattering. For energies near threshold, a combination from t-channel π^0 exchange and s-channel resonances could describe the data. For the u-channel, possible contributions could not yet be resolved. It is expected to find these contributions in the differential cross section for most backward angles of the ω meson in the center of mass frame near threshold. Published data for this kinematical region are scarce and a study with more precise data is needed. For this reason, this thesis determined the differential cross section for the most backward angular region of the $\gamma p \rightarrow \omega p$ reaction right above the ω production threshold. The BGOOD experiment in Bonn provides a suited setup for this investigation. It combines a central detector surrounding the target and a forward spectrometer, which allows for good identification of the proton.

In this thesis, the $\gamma p \rightarrow \omega p$ reaction channel was reconstructed by identifying the proton in the forward spectrometer and using cuts on the final state signature of the charged decay $\omega \rightarrow \pi^+\pi^+\pi^0$. Furthermore, a kinematic fit was applied. The yields were extracted with RooFit and cross-checked using a polynomial fit, that gave consistent yields. Based on the yield the differential cross section in the photon energy range 1109 MeV < E_γ < 1959 MeV and polar angular range $-0.99 < \cos(\theta_{\mathrm{CMS}}) < -0.9$ of the ω meson was determined.

The differential cross section against the initial photon energy starts to increase right after threshold energy and reaches a peak at around $E_\gamma \approx 1280$ MeV. Afterwards, it decreases slowly with higher energies. In comparison to other experiments, an overall agreement was observed. For the energy region 1109 MeV < E_γ < 1409 MeV the data of this analysis show higher differential cross section values than Crystal Ball data and CBELSA 2015. In higher energies, the data of this thesis overall agree to other experiments in particular with LEPS data.

The differential cross section against $\cos(\theta_{\mathrm{CMS}})$ showed a strong backward enhancement for energies below E_γ < 1450 MeV, which is not present in the data of other experiments. For higher photon energies the data points of this analysis show a flat distribution or even a decrease in differential cross section towards backward angles. This behaviour agrees mostly with LEPS data.

The strong backward enhancement in differential cross section for photon energies right above threshold might imply u-channel contribution. To verify this result and further analyse this behaviour future

research including a larger data set and incorporating the neutral decay channel is required.

Bibliography

[1] Q. Zhao,
Nucleonic resonance excitations and "missing resonances" in the ω meson photoproduction,
Nuclear Physics A **675** (2000) 217, ISSN: 0375-9474,
URL: http://dx.doi.org/10.1016/S0375-9474(00)00251-7 (cit. on p. 1).

[2] P. A. Zyla et al., *Review of Particle Physics*, PTEP **2020** (2020) 083C01 (cit. on pp. 3, 26, 27).

[3] A. Sibirtsev, K. Tsushima and S. Krewald,
Systematic Regge theory analysis of ω photoproduction, Phys. Rev. C **67** (2003) 055201,
URL: https://link.aps.org/doi/10.1103/PhysRevC.67.055201 (cit. on p. 5).

[4] P.L. Cole and F.J. Klein,
Photoproduction of ω Mesons off Protons with Linearly Polarized Photons,
URL: https://www.jlab.org/exp_prog/proposals/99/PR99-013.pdf (cit. on p. 5).

[5] J. Barth et al., *Low-energy of photoproduciton of ω-mesons*, Eur. Phys. J. A **18** (2003) 117
(cit. on pp. 7, 8, 11, 38–40).

[6] F. Klein et al., *Beam asymmetries in near-threshold ω photoproduction off the proton*,
Phys. Rev. D **78** (2008) 117101,
URL: https://link.aps.org/doi/10.1103/PhysRevD.78.117101 (cit. on p. 7).

[7] V. Vegna et al., *Measurement of the Σ beam asymmetry for the ω photoproduction off the proton and the neutron at the GRAAL experiment*, Phys. Rev. C **91** (2015) 065207,
URL: https://link.aps.org/doi/10.1103/PhysRevC.91.065207 (cit. on p. 7).

[8] M. Williams et al.,
Differential cross sections and spin density matrix elements for the reaction γp → pω,
Phys. Rev. C **80** (2009) 065208, arXiv: 0908.2910 [nucl-ex] (cit. on pp. 7, 8, 11, 38–40).

[9] M. Williams et al.,
Partial wave analysis of the reaction γp → pω and the search for nucleon resonances,
Phys. Rev. C **80** (2009) 065209,
URL: https://link.aps.org/doi/10.1103/PhysRevC.80.065209 (cit. on p. 7).

[10] F. Dietz et al., *Photoproduction of ω mesons off protons and neutrons*,
Eur. Phys. J. A **51** (2015) 6 (cit. on pp. 7, 9, 11, 37–40).

[11] A. Wilson et al., *Photoproduction of ω mesons off the proton*,
Physics Letters B **749** (2015) 407, ISSN: 0370-2693,
URL: https://www.sciencedirect.com/science/article/pii/S0370269315006127
(cit. on pp. 7, 9, 11, 37–40).

[12] I. I. Strakovsky et al., *Photoproduction of the ω meson on the proton near threshold*, Phys. Rev. C **91** (2015) 045207, URL: https://link.aps.org/doi/10.1103/PhysRevC.91.045207 (cit. on pp. 7, 10, 11, 37–40).

[13] Y. Morino et al., *Backward-angle photoproduction of ω and η′ mesons from protons in the photon energy range from 1.5 to 3.0 GeV*, PTEP **2015** (2015) 013D01, arXiv: 1306.3031 [nucl-ex] (cit. on pp. 7, 9, 11, 37–40).

[14] Q. Zhao, *Nucleonic resonance excitations with linearly polarized photons in $\gamma p \to \omega p$*, Phys. Rev. C **63** (2001) 025203, URL: https://link.aps.org/doi/10.1103/PhysRevC.63.025203 (cit. on p. 7).

[15] Y. Oh, A. I. Titov and T.-S. H. Lee, *Nucleon resonances in ω photoproduction*, Phys. Rev. C **63** (2001) 025201, URL: https://link.aps.org/doi/10.1103/PhysRevC.63.025201 (cit. on p. 7).

[16] A. I. Titov and T.-S. H. Lee, *Effective Lagrangian approach to the ω photoproduction near threshold*, Phys. Rev. C **66** (2002) 015204, URL: https://link.aps.org/doi/10.1103/PhysRevC.66.015204 (cit. on p. 7).

[17] G. Penner and U. Mosel, *Vector meson production and nucleon resonance analysis in a coupled-channel approach for energies $m_N < \sqrt{s} < 2$GeV. II. Photon-induced results*, Phys. Rev. C **66** (2002) 055212, URL: https://link.aps.org/doi/10.1103/PhysRevC.66.055212 (cit. on p. 7).

[18] I. Denisenko et al., *N^* decays to Nω from new data on $\gamma p \to \omega p$*, Physics Letters B **755** (2016) 97, ISSN: 0370-2693, URL: https://www.sciencedirect.com/science/article/pii/S0370269316000800 (cit. on p. 7).

[19] N. C. Wei et al., *Nucleon resonances in $\gamma p \to \omega p$ reaction*, Phys. Rev. D **100** (2019) 114026, URL: https://link.aps.org/doi/10.1103/PhysRevD.100.114026 (cit. on p. 7).

[20] S. Alef et al., *The BGOOD experimental setup at ELSA*, Eur. Phys. J. A **56** (2020) 104, arXiv: 1910.11939 [physics.ins-det] (cit. on pp. 13, 15, 17, 18, 25).

[21] *Electron Stretcher Accelerator (ELSA) Homepage*, URL: http://www-elsa.physik.uni-bonn.de/index_en.html (cit. on p. 14).

[22] A. Bella, *Linearly polarised photon beams at the BGO-OD experiment at ELSA*, PhD Thesis: Universität Bonn, 2016 (cit. on p. 15).

[23] S. Alef, *Scintillating fibre detector and kinematic fitting for the BGO-OD experiment*, Master Thesis: Universität Bonn, 2015 (cit. on p. 15).

[24] B.-E. Reitz, *Coherent bremsstrahlung with the scintillating fiber detector of the BGO-OD tagging system*, Master Thesis: Universität Bonn, 2015 (cit. on p. 15).

[25] G. Scheluchin, *Λ(1405) photoproduction with the BGO-OD experiment*, PhD Thesis: Universität Bonn, 2019 (cit. on pp. 16, 17, 21, 22, 33).

[26] P. Avery, *Applied Fitting Theory VI, Formulas for Kinematic Fitting*, URL: http://www.phys.ufl.edu/~avery/fitting/kinematic.pdf (cit. on p. 21).

[27] P. Avery, *Applied Fitting Theory I, General Least Squares Theory*, URL: http://www.phys.ufl.edu/~avery/fitting/fitting1.pdf (cit. on p. 21).

[28] RooFit, URL: https://root.cern.ch/doc/master/group__Roofit.html (cit. on p. 23).

List of Figures

List of Tables